PNAS RESEARCH ARTICLE | MEDICAL SCIENCES

Mitochondrial remodeling in skeletal muscle underlies exercise-induced reversal of age-associated functional decline in mice and humans

Esther García-Domínguez[a,b], Cristina García-Domínguez[a,c], José Luis Cabrera-Alarcón[d], María del Mar Muñoz-Hernández[d], Pablo Hernansanz-Agustín[e], Andrea Curtabbi[d], Julio Domenech-Fernandez[f,g], Enrique Calvo[d,h], Jesús Vázquez[d,h], Antonio L. Serrano[i], Pura Muñoz-Cánoves[i], Gloria Olaso-González[a,b,1], José Antonio Enríquez[b,d], and María Carmen Gómez-Cabrera[a,b,1]

Affiliations are included on p. 10.

Edited by David J. Glass, Regeneron Pharmaceuticals Inc, Tarrytown, NY; received April 8, 2025; accepted February 18, 2026

Loss of skeletal muscle mass and strength are common manifestations of frailty in older people and are linked to reduced quality of life. However, whether mitochondria are mechanistically linked to frailty and how physical activity, or lack thereof, is involved in age-related functional decline are still unknown. We report that exercise-induced improvements in functional capacity, including reduced frailty in old mice, are dependent on mitochondrial adaptations in skeletal muscle at structural, enzymatic, and functional levels. Our preclinical study included a healthy aging mouse line, a transgenic model of robustness, and a muscle-specific mitochondrial-deficient mutant mice, allowing us to assess both mitochondrial plasticity with aging and the necessity of intact mitochondrial function for exercise-induced adaptations. These findings were corroborated by a cross-sectional human study examining the relationship between skeletal muscle mitochondrial function, age, and physical capacity. We analyzed biopsies from 30 donors (men and women, aged 17 to 99 y) stratified into young and older adults with varying functional statuses. Our results indicate that mitochondrial dysfunction in skeletal muscle is associated with the decline in locomotor muscle function in the elderly, highlighting the potential role of exercise or habitual physical activity in mitigating this phenotype. Notably, we demonstrate that skeletal muscle mitochondria maintain plasticity during aging in mice and humans, and that this preserved adaptability can be leveraged to improve muscle performance and overall functional capacity.

frailty | sarcopenia | proteomics | health span | mitochondrial function

Significance

Maintaining functional capacity is a cornerstone of geriatric medicine and a central goal of aging research. Although human lifespan has increased, frailty and disability remain highly prevalent in older adults. Exercise benefits both cellular and systemic health, but the underlying molecular mechanisms are not fully understood, and its role in preserving mitochondrial integrity during aging remains debated. Our study provides direct evidence, in mouse models, that age-related decline in muscle function and frailty depend on mitochondrial dysfunction and demonstrates the potential of exercise to reverse these impairments. Habitual physical activity is associated with structural, functional, and enzymatic remodeling of skeletal muscle mitochondria in aging mice and humans, highlighting its therapeutic potential for preserving muscle health and promoting healthy aging.

Frailty, defined by diminished physiological reserves, is associated with adverse outcomes in older people, including disability, hospitalization, and increased mortality (1). While early detection and targeted interventions are crucial, significant research gaps remain in understanding the underlying molecular mechanisms of frailty. Regardless of its causes, skeletal muscle is the primary organ affected, as it undergoes structural (atrophy) and functional (weakness) deterioration (2) that drives the progression of frailty and its clinical consequences (3).

Mitochondrial dysfunction is a central hallmark of aging (4). Skeletal muscle cells, which have high energy demands, are susceptible to the age-related bioenergetic decline caused by the accumulation of defective mitochondria during aging (5). We recently generated the first single-cell/single-nucleus transcriptomic and chromatin accessibility map of human skeletal muscle from individuals with distinct frailty levels and have shown an age-associated accumulation of defective mitochondria in myofibers (6).

Limited data link the accumulation of defective mitochondria to phenotypic and pathological changes in aging. Indeed, not all studies have reported decreases in markers of mitochondrial content and respiratory function with aging (7), likely due to participant variability in physical activity and/or training status (8, 9). Furthermore, the difficulties in accessing human skeletal muscle biopsies in well-characterized aging cohorts have limited the scope of research in this field.

In this study, we use preclinical and clinical studies to address whether mitochondria are mechanistically linked to the functional decline associated with aging and whether muscle oxidative capacity inevitably decreases with age, independently of habitual physical activity.

Results and Discussion

To study whether the skeletal muscle of old animals retains mitochondrial plasticity, we trained a group of 20-mo-old wild-type (WT) C57BL/6 J mice (n = 20, 13 males and 7 females) for 10 wk, 5 d per week, following a high-intensity multicomponent interval

The authors declare no competing interest.

This article is a PNAS Direct Submission.

[1]To whom correspondence may be addressed. Email: gloria.olaso@uv.es or carmen.gomez@uv.es.

This article contains supporting information online at https://www.pnas.org/lookup/suppl/doi:10.1073/pnas.2508286123/-/DCSupplemental.

Published March 30, 2026.

training (HIMIT) Regimen. The training protocol included motor coordination, resistance, and high-intensity cardiorespiratory exercises (Fig. 1*A*). Following this late-onset exercise intervention, we assessed its effectiveness in reversing frailty and modulating mitochondrial function in skeletal muscle. Additionally, we included 20-mo-old G6PD-Tg mice (n = 20, 9 males and 11 females), which is an established mouse model of robustness and healthy aging that exhibits increased expression of mitochondrial complexes II to V in skeletal muscle and improved functional performance in older animals (10, 11). Nontrained WT old mice were used as controls (n = 21, 12 males and 9 females).

Body weight, energy intake, and water consumption, throughout the intervention, are shown in *SI Appendix*, Fig. S1 *A* and *B*. At baseline (preintervention), the G6PD-Tg old mice performed better in maximal running time, grip strength, and ladder-climbing force (Fig. 1 *B–E*). Postintervention measurements, 48 h after the final exercise session, revealed significant improvements in all tests, including motor coordination, for the trained WT mice compared to the sedentary WT ones. These old, trained mice matched the performance of the old, robust G6PD-Tg mice (Fig. 1 *B–E*). Furthermore, old mice in the trained group exhibited a reduced percentage of frailty (12) and increased VO_{2max}, which is a well-known marker of exercise capacity and a strong predictor of reduced mortality (13) (Fig. 1 *F* and *G*; see also accessory functional measurements, *SI Appendix*, Fig. S1 *C–E*).

As aging and lifestyle factors influence the energetic cost of movement and substrate utilization, we measured in vivo metabolic function and free-living activity using indirect calorimetry in metabolic cages at the end of the intervention (23-mo-old mice). Old, untrained mice had a higher respiratory exchange ratio (RER) and rearing activity (indicative of anxiety) compared to trained or G6PD-Tg old mice (Fig. 1 *H* and *K*). In turn, the trained mice had significantly lower ambulatory activity than the sedentary or G6PD-Tg mice yet maintained a high energy expenditure (Fig. 1 *I* and *J*). We also recorded the voluntary running activity of the mice by giving them free access to a running wheel placed in their home cage. We found increased running activity in all experimental groups during the dark (e.g., active) cycle, with no significant differences between interventions (*SI Appendix*, Fig. S1*F*). We previously reported that old mice trained with a high-intensity exercise protocol were significantly less active than the sedentary ones and that this difference may be related to the loss of body weight associated with the intervention (14).

Training significantly improved body composition in the old WT mice, increasing lean mass (Fig. 1*L*) with no changes in fat, bone area, or bone volume (*SI Appendix*, Fig. S1*G*). Hindlimb muscle weights were also recorded in both sexes (Fig. 1 *M* and *N* and *SI Appendix*, Fig. S1*H*), and the weights of the extensor digitorum longus and gastrocnemius muscles (normalized to body weight) were higher in both WT trained and G6PD-Tg old mice (Fig. 1 *M* and *N*). Improvements in muscle mass are associated with improved glucose regulation (15). We found a significant decrease in fasting glycemia in the old G6PD-Tg mice compared to the old WT sedentary ones, even though the interventions did not affect glucose tolerance (*SI Appendix*, Fig. S1 *I* and *J*). To determine whether the increase in skeletal muscle mass was accompanied by changes in fiber cross-sectional area we analyzed both parameters in the soleus muscle. We found a training-induced enlargement of fiber cross-sectional area in old animals compared with the other experimental groups (*SI Appendix*, Fig. S1*K*). Consistent with previous knowledge (6), aging induces a general decrease in the cross-sectional area of the muscle fibers which translates into functional changes. These results indicate that exercise training can partially counteract age-related alterations in muscle fiber morphology, contributing to the preservation of muscle function in old mice.

We observed a significant increase in citrate synthase activity, a well-known marker of mitochondrial mass, in quadriceps homogenates from trained and G6PD-Tg old animals (Fig. 2*A*). Greater NADH-TR staining intensities in exercised and G6PD-Tg mice also demonstrate an enhanced capacity for oxidative metabolism in these experimental groups (16) (Fig. 2*B*). This increase was accompanied by a significant decrease in blood lactate concentration following an incremental treadmill test, despite increased running distances in the same experimental groups (Fig. 2*C*). These results suggest a mitochondrial-mediated reduction in the rates of muscle glycogen depletion and lactic acid accumulation during submaximal exercise (17) in the trained and G6PD-Tg old mice. Next, we isolated mitochondria from the quadriceps muscle and found that G6PD-Tg and trained WT mice exhibited a higher CII and CIV-dependent State 3 respiration (Oxygraph-2k), compared to sedentary controls (Fig. 2*D*). This improvement was accompanied by an increase in CI, CIII, and CIV spectrophotometric maximal activities in both groups (i.e., trained and G6PD-Tg) (Fig. 2*E*). Increased CI+III and CII+III activities were only evident in the old, trained mice, as compared to the other experimental groups (*SI Appendix*, Fig. S2*A*). Although complex V activity remained unchanged (*SI Appendix*, Fig. S2 *A*, *Right* panel), maximal mitochondrial respiration stimulated by the uncoupler FCCP was significantly improved in the trained and G6PD-Tg old mice (Fig. 2*F*). We also found a significant decrease in the H_2O_2 production during maximal respiration, as measured using the fluorogenic probe Amplex Red (Fig. 2 *F*, *Right* panel) in the trained and in the G6PD-Tg mice. CI and CII dependent H_2O_2 production was not different between the experimental groups in the isolated mitochondria (*SI Appendix*, Fig. S2 *B* and *C*). However, we also found a higher mitochondrial membrane potential ($\Delta\Psi m$) in the old trained and G6PD-Tg groups using the complex II substrate succinate (CII-dependent respiration) (*SI Appendix*, Fig. S2*C*) that was not evident when we analyzed the complex I-dependent respiration (*SI Appendix*, Fig. S2*B*). Notably, $\Delta\Psi m$ plays an essential role in energy storage during oxidative phosphorylation and in mitochondrial homeostasis through selective elimination of dysfunctional mitochondria (18). Our results are consistent with previous reports (19) and show that HIMIT reverses the age-associated decline in mitochondrial respiration and membrane potential in the skeletal muscle of old mice. Our finding that the H_2O_2 emission decreases after a training period agrees with some previous studies (20) but not with all (21). Dysfunctional mitochondria, characterized by reduced oxidative phosphorylation efficiency and excessive production of reactive oxygen species (ROS), contribute to oxidize and damage macromolecules (22). We, therefore, analyzed different redox markers to test the antioxidant effects of our training protocol (23). We found that the muscle specimens of both trained and G6PD-Tg mice had significantly higher activities of G6PD, an enzyme located at the core of the antioxidant defense (24), and decreased levels of malondialdehyde (MDA), a marker of lipid peroxidation (Fig. 2*G*). These findings indicate that exercise training enhanced G6PD activity and protects against oxidative stress and macromolecular damage by reducing the accumulation of oxidized lipids.

Aging has a widespread impact on many muscle proteins (25). However, the regulation of transcription and translation in this context remains controversial (26). We, therefore, performed high-throughput skeletal muscle protein profiling to detect differentially expressed proteins across the experimental groups

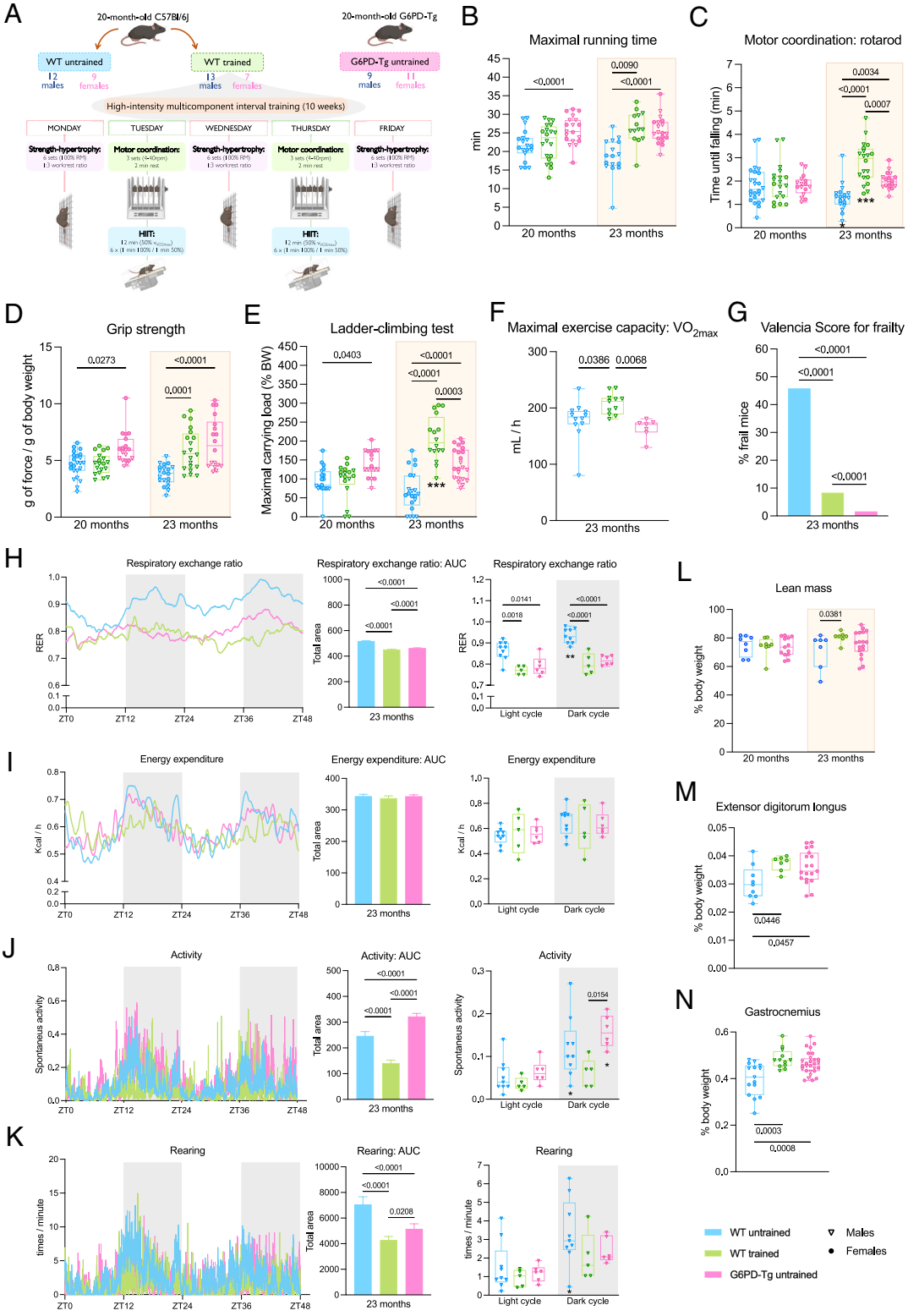

Fig. 1. Impact of high-intensity multicomponent training and G6PD overexpression on whole-body physiology and in vivo metabolism in old mice. (*A*) Schematic representation of the experimental protocol. (b-g) Physical and functional performance before and after the intervention. Maximal running time during the incremental treadmill test (*B*), motor coordination assesed by rotarod (*C*), grip strenght (*D*), maximal carrying load in the ladder-climbing test (*E*), maximal exercise capacity (VO_{2max}) (*F*), and percentage of frail mice per group (*G*). (*H–K*) In vivo metabolic assessment in female mice. Respiratory Exchange Ratio (*H*), energy expenditure (*I*), activity (*J*), and rearing (*K*) over time (48 h). Data represent the area under the curve and the average per light/dark cycle across two complete 24-h periods. Zeitgeber Time (ZT) was used to align data with the light/dark cycle, where ZT0 corresponds to lights on (08:00) and ZT12 to lights off (20:00). (*L*) Lean mass assessed through dual-energy X-ray absorptiometry. (*M* and *N*) Skeletal muscles weights. Open triangles represent data from male mice, and filled circles represent data from female mice. Baseline measurements (preintervention) are represented by empty boxes. Postintervention measurements conducted 48 h after the final exercise session are represented inside the yellow boxes. Comparisons between "Post" intervention groups (i.e., 23 mo old) and comparisons between total areas under curves were performed using a one-way ANOVA. Comparisons between "Pre" and "Post" intervention groups (i.e., 20 mo- old and 23 mo-old, respectively) were conducted using a two-way ANOVA (*** Differences pre–post, $P < 0.0001$; * Differences pre–post, $P < 0.05$). Comparisons between groups in the light and dark cycles were conducted using a two-way ANOVA (** Differences light vs dark, $P < 0.001$; * Differences light vs dark, $P < 0.05$). Abbreviations: HIIT = high intensity interval training.

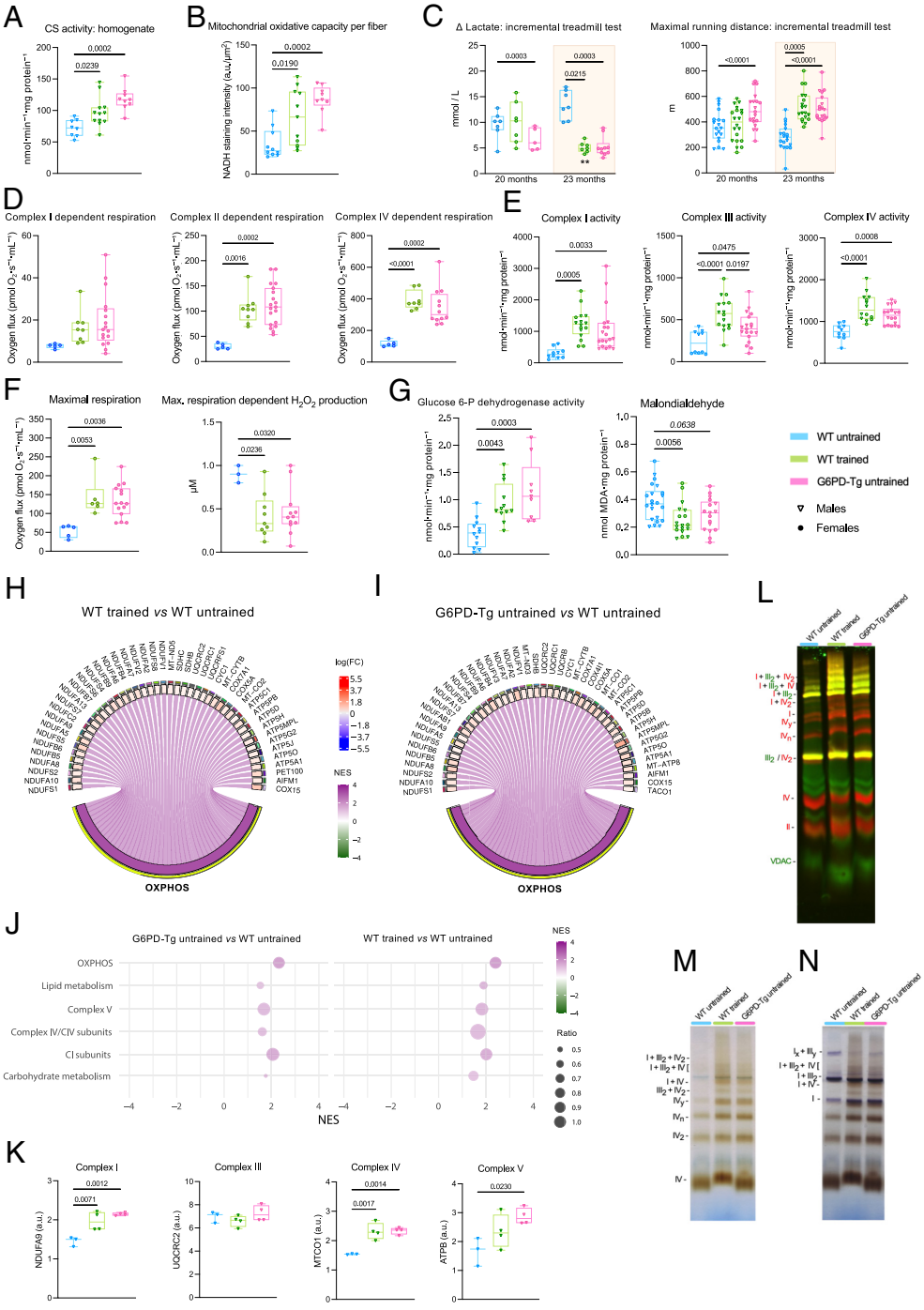

Fig. 2. An exercise intervention can rescue the age-associated decrease in mitochondrial-dependent respiration and activity in skeletal muscle. Proteomic and supercomplexes analyses in mice. (*A*) Citrate synthase activity in skeletal muscle homogenate. (*B*) Mitochondrial oxidative capacity in mouse soleus muscle sections assessed by NADH staining intensity. (*C*) Change (Δ) in peripheral blood lactate concentration and maximal running distance after an incremental running test. (*D*) High-resolution respirometry (Oxygraph-2k) in isolated mitochondria from quadriceps muscle showing Complexes I, II, and IV dependent respiration). (*E*) Mitochondrial enzymatic activities of Complexes I, III, and IV in isolated mitochondria from quadriceps muscle. (*F*) Maximal respiration and maximal respiration dependent H_2O_2 production (Oxygraph-2k) in isolated mitochondria from quadriceps muscle. (*G*) G6PD activity and malondialdehyde levels in skeletal muscle. (*H* and *I*) Chord diagrams representing selected significant gene signatures from mitocarta 3.0 in a GSEA, comparing (*H*) WT trained *vs* WT untrained, and (*I*) G6PD-Tg untrained *vs* WT untrained. The width of each arrow represents the magnitude of the association (scaled to one SD), while the color represents the direction of the effect. (*J*) Bubble plot showing selected significant gene sets from GSEA for Mitocarta 3.0 signatures comparing all groups. Dot color represents the normalized enrichment score (NES), dot size indicates the ratio (number of peptides weighted in the analysis/total number of peptides in the proteome set), and the x-axis corresponds to the NES, illustrating the direction and magnitude of enrichment. (*K*) Relative abundance of OxPhos complex subunits assessed by western blotting and normalized to SDHA in isolated mitochondria from quadriceps muscle. (*L*) Blue native gel electrophoresis of skeletal muscle digitonin-solubilized mitochondria and immunodetection of the indicated proteins. (*M*) In-gel activity of quadriceps femoris muscle mitochondria for Complex IV. (*N*) In-gel activity for Complex I (purple bands) and Complex IV (brown bands). Open triangles represent data from male mice, and filled circles represent data from female mice. Baseline measurements (preintervention) are represented by empty boxes. Postintervention measurements conducted 48 h after the final exercise session are represented inside the yellow boxes. Comparisons between "Post" intervention groups were performed using a one-way ANOVA. Comparisons between "Pre" and "Post" intervention were done using a two-way ANOVA. ** Differences pre–post ($P < 0.001$). The chord diagrams correlate differential peptide expression expressed as log(FC) with the NES. Selected mitocarta terms were identified through exploratory Gene Set Enrichment Analysis (GSEA), applying an FDR threshold of q-value < 0.25. The effect size and direction of the selected gene sets are represented by the NES. No differences between WT trained and G6PD-Tg control were found.

(See Dataset S1 and *SI Appendix*, Fig. S2*D* for information on the experimental protocol). Analysis of the MitoCarta proteome using Gene Set Enrichment Analysis (GSEA) demonstrated that exercise training and G6PD overexpression in old mice both promoted enrichment of mitochondrial OxPhos pathways (Fig. 2 *H–J*). We validated this finding by assessing mitochondrial OxPhos complex levels in skeletal muscle via western blotting. As shown in Fig. 2*K*, protein levels of complexes I and IV were significantly increased in old mice following either training or G6PD overexpression.

We also performed an RNA-seq analysis that confirmed the proteomic results, highlighting mitochondrial-based metabolic processes, such as enhanced OxPhos activity and increased cristae formation in the trained and G6PD-Tg groups. According to these data, we also found an upregulation of ROS detoxification and glutathione metabolism genes in both the trained and the G6PD-Tg groups (*SI Appendix*, Fig. S2*E* and Dataset S2).

Aging is closely linked to mitochondrial complex enzyme assembly defects, which hold significant biological and biomedical importance (27). To investigate for differences in mitochondrial complex organization, we next examined the structural and functional assembly of mitochondrial complexes and supercomplexes using Blue Native gel electrophoresis followed by immunodetection of proteins (Fig. 2*L*) and in-gel activity (Fig. 2 *M* and *N*) assays (28). Our findings revealed increased formation of mitochondrial respiratory supercomplexes in trained and G6PD-Tg old mice. Therefore, the HIMIT protocol promoted favorable adaptations in WT mice by enhancing supercomplex assembly. These results indicate that exercise training improves mitochondrial adaptability at the molecular, cellular, and metabolic levels in old skeletal muscle, highlighting that mitochondria retain a remarkable degree of plasticity during aging in mice.

To test whether these mitochondrial adaptations are functionally required for exercise-induced benefits per se, we next limited mitochondrial OxPhos capacity in skeletal muscle using a muscle-specific *Usmg5* knockout model. *Usmg5* encodes *DAPIT*, a mitochondrial ATP synthase subunit essential for efficient oxidative phosphorylation. Muscle-specific deletion of *Usmg5* enables genetic testing of the role of mitochondrial function in exercise-induced adaptations (29). In contrast to WT mice, Usmg5 mKO trained animals failed to elicit the expected enhancement of mitochondrial oxidative capacity (*SI Appendix*, Fig. S2*F*), exhibited increased reliance on fermentative metabolism during exercise, and did not improve physical performance following training Fig. 2*G*. These findings indicate that intact mitochondrial OxPhos capacity is an important determinant for the physiological and functionally meaningful benefits of exercise in mice.

To investigate the relationship between physical performance and mitochondrial function in human aging, we recruited a cohort of 30 adults (13 males and 17 females) divided into two age groups: younger adults [n = 8; 5 men and 3 women; 37.3 (10.6) y], and older adults [n = 22; 8 men and 14 women; 86.7 (9.7) y]. Participants were characterized based on anthropometric data, self-reported levels of physical activity, and three geriatric scales: Barthel (30), Charlson (31), and the modified 5-item Frailty Index (32) (Fig. 3 *A* and *B* and *SI Appendix*, Fig. S3 *A* and *B*). The younger adults outperformed the older groups in all the geriatric scales (Fig. 3 *B*; *Left* segment of the heatmap). We then divided the older adults into two functionally different groups: older with poor physical function (OPF) [n = 11; 4 men and 7 women; 86.7 (9.7) y], who performed poorly across most tests (middle of the heatmap); and older with good physical function (OGF) [n = 11; 4 men and 7 women; 84.7 (7.2) y], who performed significantly better than the OPF group (right segment of the heatmap). Both older groups were matched for age, sex, and BMI (Fig. 3*A* and *SI Appendix*, Fig. S3*A*). Thus, our experimental conditions were ideal for studying the role of mitochondria in age-related physical performance decline.

We collected skeletal muscle biopsies from all participants from the hip muscles, which are clinically important due to their role in pelvic stabilization, postural control, and fall prevention [as falling can lead to severe complications in older adults (33)] (see Fig. 3*C* for information on the experimental protocol). Using the muscle specimens, we first confirmed the age-associated skeletal muscle atrophy (*SI Appendix*, Fig. S3*C*). Histochemical SDH staining revealed a decrease in the myofiber respiration capacity in the OPF group compared to the age-matched OGF group (*SI Appendix*, Fig. S3*D*). This finding was supported by a significant reduction in citrate synthase activity, a marker of mitochondrial mass (34), in the OPF group as compared to the other groups (Fig. 3*D*). Using isolated mitochondria from muscle specimens, we found that complex I and II-dependent respiration (Oxygraph-2k) and maximal activities were significantly higher in the OGF group compared to the OPF one. Furthermore, mitochondria from the OPF group showed a significant decrease in complex IV-dependent respiration and maximal activity compared to the younger group. However, this age-associated trend in complex IV was not statistically significant in the OGF group (Fig. 3 *E* and *F*). Greater NADH-TR staining intensity in the OGF group compared with the OPF group also indicates an enhanced oxidative metabolic capacity in old individuals who maintained their physical function (Fig. 3*G*).

We then assessed cellular oxidative stress and damage in skeletal muscle. As a marker of oxidation products, we quantified the lipid peroxidation markers (MDA and 4-HNE) and protein carbonyls (Fig. 3*H* and *SI Appendix*, Fig. S3 *E* and *F*). Although the results showed high variability, the OGF group maintained lower levels of oxidative damage, comparable to those of young adults. Additionally, we found a significant decrease in the activity of G6PD (a central antioxidant enzyme (10) in the OPF group when compared to the young and OGF groups.

We performed a factor analysis of mixed data (FAMD) with the functional, anthropometric, mitochondrial, and redox measurements to explain the dataset's variance and to analyze individual similarities. Our results clearly show three differentiated groups. The two main dimensions (x-axis = Dim1, and y-axis = Dim2) of the FAMD explained more than 50% of the variability in the data (54.4%) (Fig. 4*A*; see also information shared between the variables and the main dimensions, *SI Appendix*, Fig. S4 *A* and *B*). Physical activity was one of the main contributing functional variables to Dim1. Strikingly, the main contributing biochemical variables to this dimension were the G6PD and CII activities (*SI Appendix*, Fig. S4*A*). CIV-dependent respiration contributed most to Dim2 (*SI Appendix*, Fig. S4*B*). A correlation heatmap revealed significant associations between all the measurements (Fig. 4*B*). A relevant aspect of our study is that CII activity and physical activity exhibited the strongest associations with the rest of the variables, followed by the Barthel index and G6PD activity (Fig. 4*B* and *SI Appendix*, Fig. S4*C*). In particular, physical activity correlated significantly with improvements in functional parameters (Frailty, Barthel, and Charlson indices), mitochondrial volume, and respiratory capacity (i.e. complex I–IV dependent respiration and complex I and II activities). Likewise, the G6PD and CII activities were strongly associated with all functional parameters, as their increase was associated with a significant decrease in frailty, dependency, and comorbidities (see *SI Appendix*, Fig. S4*D* and Dataset S3 for Pearson correlation coefficients (r) between the analyzed variables).

Finally, we performed a high-throughput protein profiling in skeletal muscle extracts enriched in mitochondria to better

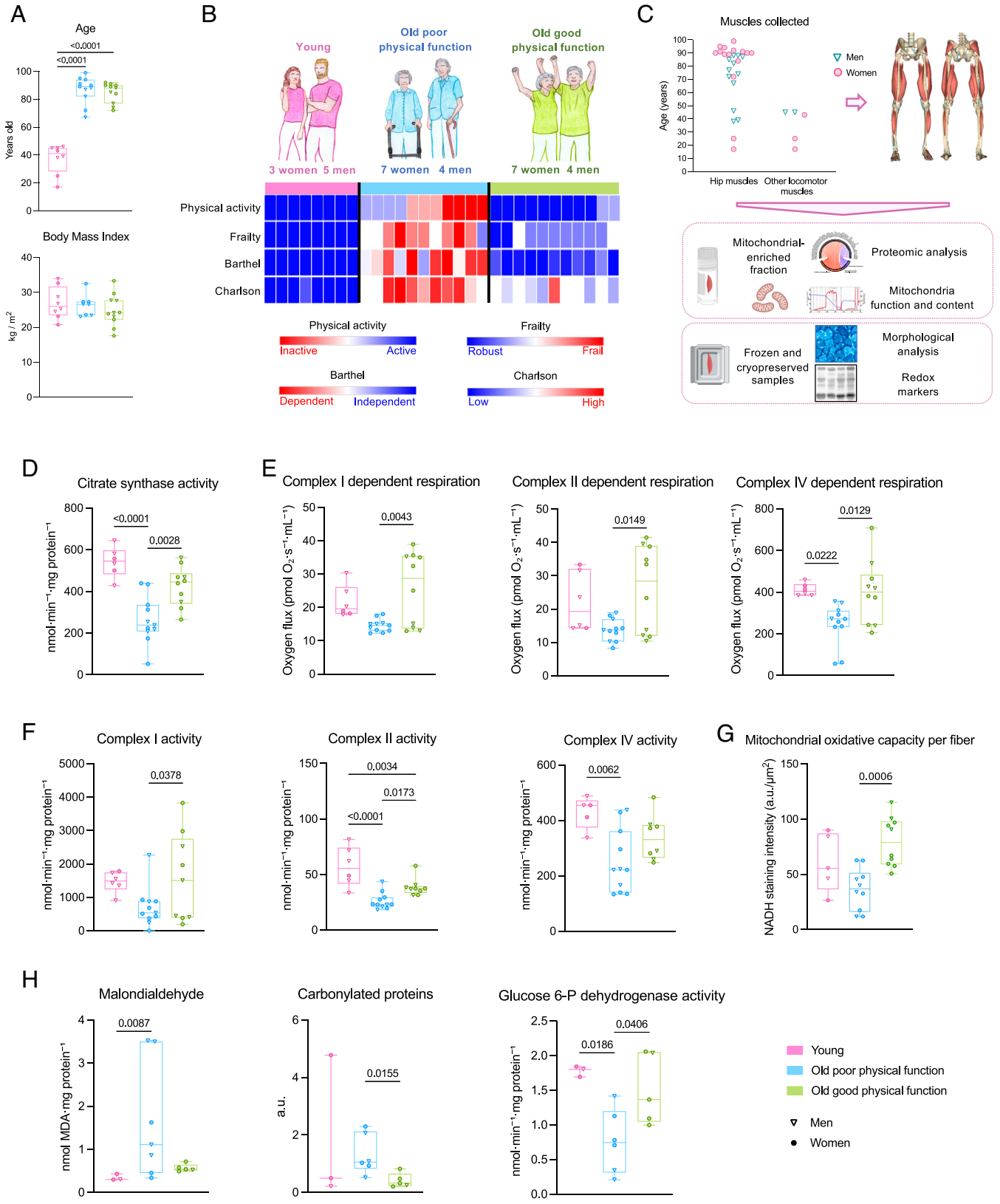

Fig. 3. Mitochondrial-dependent respiration and activity in human skeletal muscle decline with age and are influenced by the individual's functional status. (*A*) Age, and body mass index of the donors. (*B*) Sample characterization. The heatmap represents the performance in the indexes/scales included in the functional characterization. In the color scale, blue and red represent excellent and poor performance, respectively, with the transition (white) at the overall mean. (*C*) Representation of the muscles collected based on age and sex, sample processing, and the analyses performed. (*D*) Citrate synthase activity as a marker of mitochondrial mass. (*E*) Mitochondrial respiration (Oxygraph-2k) through Complexes I, II, and IV in a mitochondria-enriched muscle fraction following three freeze-thaw cycles. (*F*) Mitochondrial enzymatic activities of Complexes I, II, and IV in a mitochondria-enriched muscle fraction. (*G*) Mitochondrial oxidative capacity in mouse soleus muscle sections assessed by NADH staining intensity. (*H*) Skeletal muscle oxidative damage markers (MDA and protein carbonyls, normalized to total proteins) and G6PD activity. Open triangles represent data from men, and filled circles represent data from women donors. All comparisons between groups were performed using the Kruskal–Wallis test.

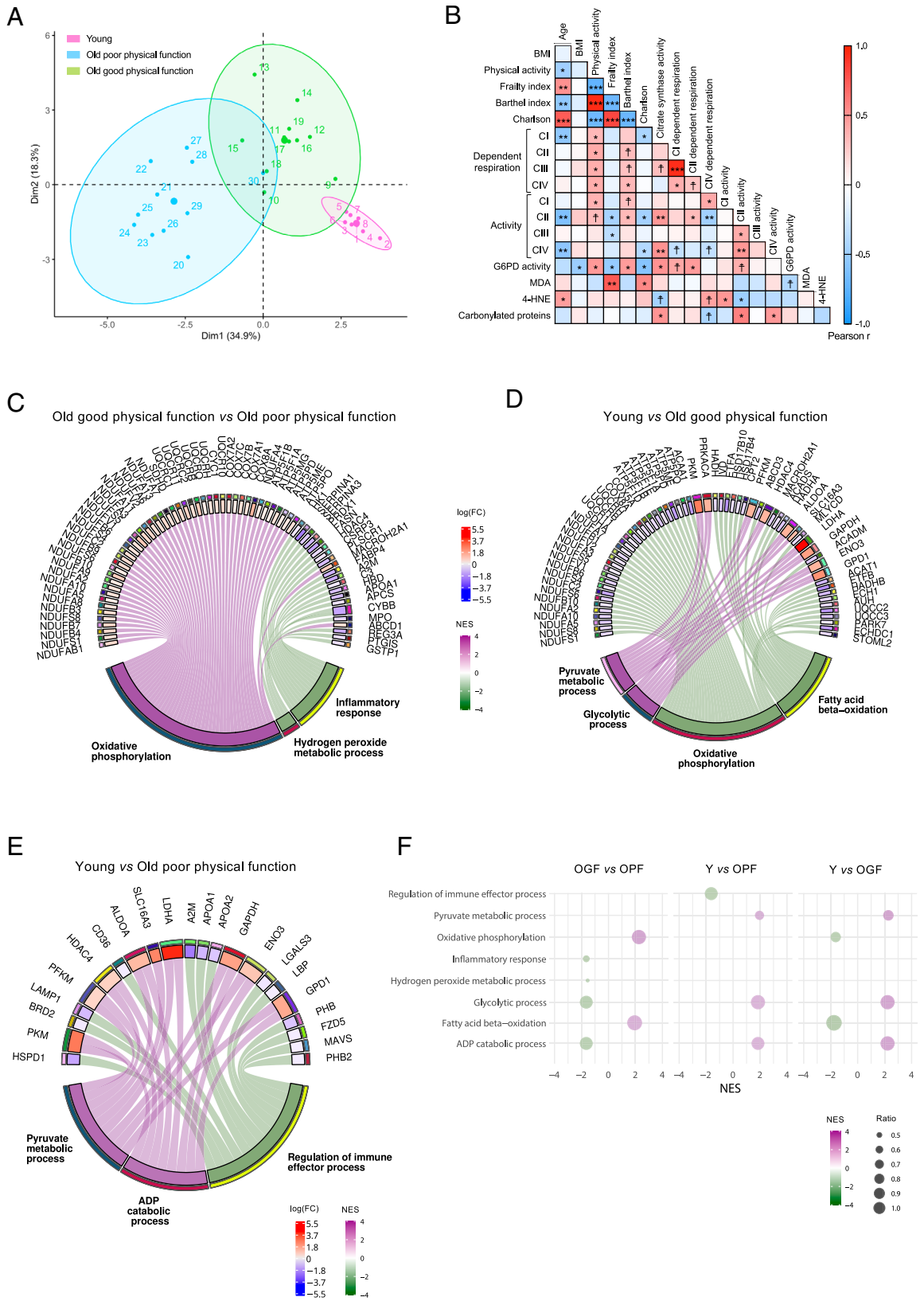

Fig. 4. Association between quantitative and qualitative variables in the human study and proteomic analysis in mitochondrial enriched fractions from human skeletal muscles. (*A*) Factor analysis of mixed data (FAMD). Individuals are plotted in a two-dimensional PCA space, with groups clustered based on the first two principal components (Dim1 and Dim2): pink (Y), blue (OPF), and green (OGF). Percentages indicate the variance explained by each dimension, and confidence ellipses illustrate group variance. (*B*) Pearson correlation coefficients (r) computed in a correlation matrix. Positive correlations are displayed in red, and negative ones in blue. The symbols inside the boxes indicate the *P*-value of the corresponding correlation: $^{*}P < 0.05$; $^{**}P < 0.01$; $^{***}P < 0.001$; $^{\dagger}P < 0.1$. (*C–E*) Chord Diagrams representing the differentially regulated proteins in our experimental groups using GO terms and GSEA comparing: (*C*) OGF *vs* OPF, (*D*) Y *vs* OGF, and (*E*) Y *vs* OPF. (*F*) Bubble plot showing selected significant GO Biological Process gene sets from GSEA of MitoCarta 3.0 signatures comparing all groups. Dot color represents the NES, dot size indicates the proportion of peptides contributing to each term relative to the total proteome set, and the x-axis shows NES, illustrating the direction and magnitude of enrichment. Abbreviations: Y = Young, OGF = Old good physical function, OPF = Old poor physical function.

understand which mitochondrial proteins were associated with the maintenance of skeletal muscle function during aging (see *SI Appendix*, Fig. S4*E* for details). We quantified 877 proteins, among which we found overexpression of those related to OxPhos in the OGF group, consistent with an increase in mitochondrial volume and improved respiratory capacity (Fig. 4*C* and Dataset S4). Consistent with previously reported results on oxidative damage markers, proteins involved in H_2O_2 metabolic processes were downregulated in the OGF compared to the OPF group. Additionally, in line with the inefficient compensation for increased ROS production, the inflammatory response was activated in the OPF group (Fig. 4*C*). During normal aging, the primary energy source shifts from increased glucose consumption to enhanced fatty acid oxidation (Fig. 4 *D* and *E*). This shift aligns with the general decrease in type II fibers and the relative increase in type I fibers, as we recently reported (6).

Notably, the most activated process in the OPF compared to the young group was the regulation of immune effector processes while muscle energy metabolism (including pyruvate and glucose metabolism) was downregulated (Fig. 4*E*). Blood analyses revealed alterations in immune cell-type composition (including total monocyte counts, hemoglobin, hematocrit, and platelets) in old *vs* young groups, reaching statistical significance in OPF, suggesting age-related inflammatory changes in the circulation, which may impact peripheral tissues and contribute to chronic low-grade inflammation (35, 36) (*SI Appendix*, Fig. S4*F*). Finally, the proteomic results were consistent with phenotypic and molecular signatures indicating respiratory-competent mitochondria in the young and OGF vs OPF groups (Fig. 4*F*).

In both mice and humans, pathways related to oxidative phosphorylation and lipid/fatty acid metabolism were enriched in the older higher fitness groups (OGF, G6PD-Tg, and WT trained), suggesting a conserved mitochondrial and metabolic remodeling, with notable similarities between the OGF humans and G6PD-Tg animals, our mouse model of healthy aging. In contrast, glycolytic pathway enrichment showed a divergent pattern: in humans, higher glycolytic activity was observed in the OPF group, while in mice this shift was less prominent. Notably, we have recently reported that, in old humans, type I myonuclei undergo metabolic reprogramming toward a more glycolytic phenotype, probably counterbalancing the loss of oxidative capacity in type I myofibers. This adaptive shift may represent a compensatory mechanism to sustain ATP production when mitochondrial oxidative phosphorylation becomes compromised in the OPF group (6). Furthermore, inflammatory and immune-related processes were selectively enriched in older humans with poor function but not in the mouse study, indicating that chronic low-grade inflammation may be a more dominant driver of functional decline in humans than in the controlled murine environment.

While accumulating evidence supports the beneficial effects of exercise on cellular and organismal health, the underlying molecular mechanisms remain largely speculative, particularly regarding its role in preserving mitochondrial integrity during aging. Our study establishes a link between the decline in locomotor muscle function and frailty in older individuals and mitochondrial dysfunction. It underscores the significant impact of regular physical activity on functional capacity and mitochondrial adaptability in aging. These findings provide compelling evidence that mitochondria retain plasticity throughout aging, both in mice and humans.

Materials and Methods

Study Population and Donor Sample Ethics. Thirty patients (8 young adults and 22 older adults) undergoing trauma or orthopedic surgery participated in this study from whom muscle biopsy samples were taken during the surgery. Their functional states were assessed to classify the old group into older adults with good physical function (n = 11) or older adults with poor physical function (n = 11). We used the Barthel Index (30) (to estimate the degree of dependency from 0: dependent to 100: independent), the Charlson Index (31) (to classify the grade of comorbidities from 0: without comorbidity to 6: the individual with a higher number of comorbidities), and the modified 5-item Frailty Index (32). A physician reviewed each patient's clinical history and assessed preoperative physical activity using a 4-point scale: 1, sedentary and dependent; 2, wheelchair user with partial independence; 3, ambulatory with assistance; and 4, independently ambulatory and physically active.

Exclusion criteria included myopathy, hemiplegia or hemiparesis, autoimmune connective tissue disorders, inability to consent, recent hospitalization, or major surgery within the previous three months. All participants provided written informed consent, and the study was approved by the Ethical Committee of the Department of Health Arnau de Vilanova-Liria, Spain (CEIm 28/2019).

Experimental Models and Ethics. Cohorts of 20-mo-old C57BL/6 J (wild-type, WT) and G6PD-Tg mice, both females and males, were used to study the effects of a HIMIT program on physical function, mitochondrial parameters, and molecular determinations. Twenty-five male C57BL/6 J mice were randomized into untrained (n = 12) or trained (n = 13) groups and compared with 9 untrained G6PD-Tg male mice. Sixteen female C57BL/6 J mice were randomized into untrained (n = 9) or trained (n = 7) groups and compared with 11 untrained G6PD-Tg female mice. In addition, muscle-specific *Usmg5* knockout mice (*Usmg5*$^{fl/fl}$; MCK-Cre), generated in the laboratory of JA Enriquez on a C57BL/6 J-OlaHsd background, were used to study whether intact mitochondrial function is required for exercise-induced functional benefits. Six-month-old Usmg5 mKO mice (n = 5; 3 males, 2 females) underwent a 4-wk HIIT treadmill protocol and were compared with age-matched trained WT mice (n = 5; 3 males, 2 females).

All animals were housed in groups on 12-h light/dark cycles at 24 ± 2 °C, and food and water were provided ad libitum. Mice were fed the Teklad Global 14% Protein Rodent Maintenance Diet. This diet has an energy density of 2.9 kcal/g corresponding to an energy distribution of 20% protein, 13% fat, and 67% carbohydrate.

The study followed EU guidelines for the ethical care of experimental animals and was approved by the University of Valencia Ethics Committee for Research and Animal Welfare (license 2022 VSC PEA 0035, type 2).

Exercise Training Protocol. The HIMIT protocol included strength, motor coordination, and cardiorespiratory training (Fig. 1*A*). Mice trained five days per week for 10 wk, performing strength training three days per week on an 80° inclined ladder (1 × 0.18 m, 1 cm grid), completing six climbs per session with a 1:3 work-rest ratio. Loads attached to the tail were progressively increased from 75 to 200% of the individual maximal carrying capacity. Motor coordination was trained twice per week using a rotarod (3 trials/session, 4 to 40 rpm over 5 min), and cardiorespiratory fitness was trained on a treadmill (5° incline) using a HIIT protocol consisting of a 12-min warm-up followed by six 1-min intervals at 100% vVO_2max interspersed with 1-min recovery at 50% vVO_2max.

In a second study, mice performed treadmill HIIT three days per week for four weeks (5° incline), with each session consisting of 15 bouts of 2 min at 75% of maximal running velocity separated by 2 min of passive recovery; intensity was readjusted after two weeks. All training sessions and functional assessments were conducted between 9:00 and 11:00 a.m. to minimize circadian variability.

Assessment of Physical and Functional Status in Mice. All animals were evaluated before and after the intervention and were acclimated to all the tests performed with two habituation sessions before the evaluation.

Frailty Assessment: Valencia Score. Frailty was assessed in mice using the "Valencia Score" (12), which is based on the human frailty criteria developed by Linda Fried and coworkers (37).

Body weight. Body weight was recorded weekly using a PB3002 Delta Range balance (Mettler Scales, Toledo, OH).

Grip strength. Maximal grip strength was evaluated by using the Grip Strength Meter (Panlab, Harvard Apparatus). Relative grip strength was determined by dividing grip strength by the animal's weight.

Motor coordination. We used the rotarod (Panlab, Harvard Apparatus) to evaluate the animals' motor coordination. Each animal performed three attempts with five

minutes of rest between them. The final data recorded were the maximal time achieved in any of the tests.

Maximal oxygen consumption. Maximal oxygen consumption (VO_2max) was measured using a motorized mouse treadmill coupled to an indirect calorimetry system (Panlab, Harvard Apparatus; Oxylet Pro LE405) during an incremental exercise test (38). Blood lactate levels were measured before and 5 min after the test.

Maximal Carrying Load: Ladder-Climbing Test. Maximal carrying load was assessed using a modified ladder-climbing test (39). Mice climbed an inclined ladder (80°) with progressively increasing tail-attached loads starting at 75% of body weight and increasing by 25% until failure (three unsuccessful attempts to climb two-thirds of the ladder). The highest successful load was recorded as a percentage of body weight.

Grid-Hanging Test. Muscle strength and hanging endurance were assessed using a 30 cm^2 grid, recording latency to fall in three trials with 5-min rests; the longest time was used for analysis.

Endurance Capacity: Continuous Treadmill Test. From the maximal running speed with VO_2max (v_{VO2max}) obtained in the incremental treadmill test, mice performed a continuous running treadmill test to evaluate their endurance. After an incremental warm-up period of seven minutes, each mouse ran at 75% of its v_{VO2max}. Total running distance to exhaustion (in meters) was registered.

In Vivo Metabolic Assessment. Indirect calorimetry was performed using the OxyletPro System (Panlab, Harvard Apparatus). Data acquisition and analysis were conducted using the METABOLISM software. The following parameters were quantified: RER, EE, spontaneous physical activity, and rearing events. Mice were single-housed under controlled conditions (12-h light/dark cycle, lights on 08:00–20:00; ambient temperature 24 ± 2 °C) with ad libitum access to food and water. Prior to data collection, animals were acclimated to the metabolic cages for 24 h. Measurements were recorded every 12 min over a 48-h period. Zeitgeber Time (ZT) was used to align data with the light/dark cycle, where ZT0 corresponds to lights on (08:00) and ZT12 to lights off (20:00).

Basal Glycemia and Glucose Tolerance Test. Basal glycemia and glucose tolerance were assessed after 6 h of fasting. Basal blood glucose was measured with a glucometer, followed by intraperitoneal injection of 20% glucose (2 g/kg) and serial blood glucose measurements up to 180 min.

Body Composition: Dual X-Ray Absorptiometry. Mouse body composition was assessed by DEXA (InAlyzer, Medikors) under isoflurane anesthesia.

Human Skeletal Muscle and Blood Samples Processing. Muscle biopsies were obtained during surgery from healthy, noncontused areas using scalpel dissection along fiber orientation without electrocautery. Samples were either fixed in 2% paraformaldehyde, cryoprotected, embedded in OCT, and frozen for immunohistochemistry, or snap frozen in liquid nitrogen. Fasting blood samples were collected by antecubital venipuncture and analyzed using standardized automated procedures in the hospital's clinical laboratory.

Mice Muscle Sample Processing. Mice were killed by cervical dislocation, and hind limb skeletal muscles were dissected and weighed. Muscles were snap frozen in liquid nitrogen, except for one soleus fixed in 2% paraformaldehyde and one quadriceps preserved at 4 °C for assessment of coupled mitochondrial oxidative phosphorylation.

Glucose 6-Phosphate Dehydrogenase Activity. G6PD activity was studied in homogenates from human muscle biopsies and mouse gastrocnemius, as described by Waller and coworkers (40).

Oxidative Damage Markers.

Malondialdehyde levels. Lipid peroxidation was determined as malondialdehyde (MDA) in homogenates from human muscle biopsies and mouse gastrocnemius using HPLC as described previously (11).

Carbonylated proteins. Protein carbonylation in homogenates from human muscle biopsies was assessed using the Oxyblot Protein Oxidation Detection Kit (Millipore, USA) as previously described (11).

Mitochondria Analysis. Mitochondria were isolated from 70 mg of human muscle biopsy tissue and from the entire quadriceps femoris muscle of each mouse. The mouse muscle was immediately cooled to 4 °C in Frezza medium (67 mM Sucrose, 50 mM KCl, 50 mM Tris-HCl, 10 mM EDTA, 1 mg/mL BSA pH 7.4). The samples were mechanically disaggregated with a scalpel in a Petri dish, trypsinized for 30 min at 4 °C (0.05% Trypsin, 10 mM EDTA in PBS, pH 7.4) and homogenized in Frezza medium with a glass tissue grinder using a motor-driven Teflon pestle (Heidolph RZR 2041) with 20 strokes at 600 rpm. Then, the samples were centrifuged for 5 min at 4 °C and 1,000×*g*, and the resulting supernatant was centrifuged for 10 min at 4 °C and 10,000×*g*. Finally, the mitochondria-containing pellets were resuspended with Frezza medium.

In the human samples, mitochondria were isolated from frozen skeletal muscle (41). We followed the protocol described in the previous paragraph but used A medium (0.32 M Sucrose, one mM EDTA, ten mM Tris-HCl, pH 7.4) instead of the Frezza medium. Moreover, isolated mitochondria were frozen and thawed three times for all the mitochondrial analysis.

High-Resolution Respirometry.

Mitochondrial respiration. Mitochondrial respiration was assessed using 40 μg of mouse mitochondrial extract per chamber in an Oxygraph-2k (Oroboros) with MiR05 at 37 °C under normoxic conditions, following the SUIT 8 protocol (11).

For human samples, 6 μg of freeze–thawed mitochondrial extract were analyzed in duplicate in an O2k respirometer with MiR05 at 37 °C.

Complex I activity was measured with NADH and cytochrome c and corrected for rotenone inhibition, followed by assessment of complex II (succinate) and complex IV activities (TMPD/ascorbate), with antimycin A and azide used for inhibition.

Median oxygen flow levels for each measurement were collected using DatLab 4 software (Oroboros Instruments).

Hydrogen peroxide production. The measurement of the hydrogen peroxide production was simultaneous with respiration in fresh mice isolated mitochondria in the O2k-FluoRespirometer. It was measured fluorometrically after adding diethylenetriaminepentaacetic acid (DTPA) (15 μM), superoxide dismutase (SOD) (5 μ/mL) and horseradish peroxidase (HRP) (1 μ/mL) and doing a calibration standard of hydrogen peroxide (step increase of 0.1 μM) by using Amplex UltraRed (AmR) (10 μM) and the Fluorescence-Sensor Green (O2k-Series D-G: O2k-Fluo LED2-Module). We followed a modified SUIT 8 protocol since colored substances may influence the fluorescence signal of AmR when injected into the O2k-Chamber.

Mitochondrial membrane potential. The measurement of the mitochondrial membrane potential was simultaneous with respiration in fresh mice isolated mitochondria in the O2k-FluoRespirometer. It was measured fluorometrically after calibrating the raw fluorescence signal expressed as [V] and converted to μM by using the fluorophore tetramethylrhodamine methyl ester (TMRM) and the Fluorescence-Sensor Green (O2k-Series D-G: O2k-Fluo LED2-Module). We followed a modified SUIT 8 protocol as previously mentioned.

Citrate Synthase Activity. Citrate synthase activity was determined spectrophotometrically as a marker of mitochondrial mass as previously described (42).

Activities of the OxPhos Complexes. The activities of the five OxPhos enzymes and the mitochondrial glycerol-3-phosphate dehydrogenase (GPDH) activity were measured spectrophotometrically in isolated mitochondria from mice using a total of 5 to 20 μg of mitochondrial protein to determine the activity of each complex (43). Complex II and IV activities were also studied in 20 to 30 μL of muscle homogenate from the same extract used to isolate mitochondria (before performing the last spin).

Blue Native PAGE. Supercomplex levels and composition were studied in isolated mitochondria from skeletal muscle (20 μg) by blue native electrophoresis as described previously (28). Membranes were sequentially probed with primary antibodies to complex I (anti-NDUFA9, Abcam), complex II (anti-SDHA, ThermoFisher), complex III (anti-UQCRC2, ProteinTech), and complex IV (anti-COI, Invitrogen). VDAC1 (abcam) was used as a loading control.

Enzymatic In-Gel Activity. Determination of the enzymatic in-gel activity of different OxPhos complexes was conducted as previously reported (44). We followed the same protocol as for Blue Native PAGE, but without transferring the proteins to a membrane.

Western Blotting of Mitochondrial OxPhos Complexes. To assess the relative abundance of OxPhos proteins, SDS-PAGE and western blotting were performed in mitochondrial fractions (20 μg of protein per lane) (11).

Proteomics.

Sample Preparation. Muscle protein extracts from mouse gastrocnemius and mitochondria-enriched human samples were prepared by bead-based homogenization in CS buffer supplemented with protease and phosphatase inhibitors. Proteins (~200 μg) were reduced, alkylated, and digested overnight with trypsin using a filter-aided protocol. Peptides were desalted, quantified by Direct Detect IR, and TMT-labeled according to the manufacturer's instructions (45).

Liquid Chromatography–Tandem Mass Spectrometry (LC–MS/MS). Labeled peptides were separated on an Evosep One HPLC using Evotips and an Endurance column, and analyzed on an Orbitrap Eclipse Tribrid mass spectrometer. MS data were acquired in TopSpeed mode with Orbitrap MS (60,000 resolution) and HCD MS/MS (30,000 resolution), with dynamic exclusion set to 20 s.

Protein identification and quantification. For peptide identification, MS/MS spectra were searched using the SEQUEST HT algorithm implemented in Proteome Discoverer 2.1 (Thermo Scientific) (46) against a UniProt (47) database comprising mouse protein sequences (mouse_202105_sw.target-decoy.fasta, 185234 sequences in total) concatenated with decoy sequences generated using DecoyPyrat (48). Trypsin digestion was set with a maximum of 2 missed cleavages. Cys carbamidomethylation (57.021464 Da) and TMT labeling at the N-terminal end and Lys (304.2071 Da) were set as fixed modifications and Met oxidation (15.994915 Da) as dynamic modifications. Precursor mass tolerance was set at 800 ppm, fragment mass tolerance was at 0.03 Da, and precursor charge ranged from 2 to 4. The false discovery rate (FDR) was calculated using the corrected Xcorr score (cXcorr) (49) and the target/decoy competition strategy applying the picked FDR method at the peptide level (50), with an additional filter for precursor mass tolerance of 15 ppm (51). A 1% FDR was employed as the criterion for peptide identification.

The quantitative information derived from TMT reporter intensities was integrated from the spectrum level to the peptide level and subsequently to the protein level, according to the WSPP model (52) and the Generic Integration Algorithm (53), using the iSanXoT program (54). In this model, quantitative protein values are expressed using the standardized variable Zq (i.e., normalized $\log_2$-ratios expressed in SD units according to the estimated variances).

RNA-seq. Total RNA from mouse gastrocnemius muscle was extracted with TRIzol and purified using RNeasy columns. RNA integrity and quantity were assessed with an Agilent 2100 Bioanalyzer. RNA-seq libraries were prepared from 50 ng RNA using the NEBNext Ultra II Directional kit, including poly(A)+ selection, fragmentation, cDNA synthesis, adaptor ligation, and PCR amplification, and sequenced at the CNIC Genomics Unit.

Library size and concentration were assessed using an Agilent 2100 Bioanalyzer and Qubit fluorometer. Libraries were sequenced on a NextSeq 2000 (Illumina) to generate 61-bp single-end reads. FASTQ files were generated with bcl2fastq v2.20, adapter-trimmed with Trim Galore v0.6.6, and aligned to the mouse genome and transcriptome (Ensembl GRCm38.v91) using STAR v2.5.1. (55) and RSEM v1.3.1 (56). Genes with less than ten counts per million in the sample were filtered out. Then, expected counts were TMM-normalized using edgeR v-3.36.0. (57). Differentially expressed genes between groups were identified using the limma v-3.50.3 bioconductor package (58). Functional analysis was performed as GSEA using ClusterProfiler v-4.2.2 bioconductor package (59). GSEA for mitopathways, based on information retrieved from Mitocarta v3, was done using DOSE v-3.20.1 (60).

Histology and Histochemical Analysis. Transverse serial cryosections were obtained from skeletal muscle samples of both mice (soleus) and human biopsies using a cryostat (Microm HM 505 N) maintained at −25 °C. Cryosections were stained with hematoxylin/eosin (H&E) to evaluate muscle fiber morphology and measure cross-sectional area (CSA). NADH-tetrazolium reductase and succinate dehydrogenase staining were performed using standard protocols (6).

Statistical Analysis. All experiments and analyses were performed blinded. Sample size was calculated with G*Power (power = 0.8, $\alpha = 0.05$), and mice were pair-matched to ensure baseline equivalence. Analyses were conducted using SPSS 27, with data visualization in GraphPad Prism 10 and R 4.5.0. Data are presented as mean ± SD, with $P < 0.05$ considered significant.

Normality and homoscedasticity were assessed using Kolmogorov–Smirnov and Levene's tests, respectively. Parametric or nonparametric tests (Kruskal–Wallis) were applied as appropriate. Comparisons used t-tests, one-way ANOVA, or two-way ANOVA (group × time), followed by Bonferroni-corrected post hoc tests. Sexes were analyzed separately.

Correlations were assessed using Pearson's r, frailty scores with chi-squared tests, and multivariate analyses by FAMD. Functional enrichment was performed by GSEA using Mitocarta 3.0 gene sets on proteomic and RNA-seq data (FDR $q < 0.25$).

Data, Materials, and Software Availability. The RNA-seq data have been deposited in the NCBI Gene Expression Omnibus (GEO) under accession number GSE325919 (61). The mass spectrometry proteomics data have been deposited to the ProteomeXchange Consortium via the PRIDE partner repository with the dataset identifier PXD076192 (62). All other data are included in the article and/or supporting information.

ACKNOWLEDGMENTS. We thank all the patients who have participated in the study and the members of our teams for technical help and discussions. Work in M.C.G-C. laboratory was supported by the following Grants: Instituto de Salud Carlos III CB16/10/00435 (CIBERFES); PID2022-142470OB-I00 and Red EXERNET-RED DE EJERCICIO FISICO Y SALUD (RED2022-134800-T) from the Spanish Ministry of Science, Innovation, and Universities; PROMETEO (CIPROM/2022/56) from Consellería de Educación, Universidades, y Empleo de la Generalitat Valenciana. Part of the equipment has been funded by Generalitat Valenciana and cofinanced with FEDER funds (OP FEDER of C.V. 2014–2020). A.C. was supported by the European Union's Horizon 2020 research and innovation program under the Marie Skłodowska-Curie grant agreement n. 713,673.

Author affiliations: [a]Freshage Research Group, Department of Physiology, Faculty of Medicine, University of Valencia, Fundación Investigación Hospital Clínico Universitario/Incliva Fundación Investigación Hospital Clínico Universitario, Valencia 46010, Spain; [b]Centro de Investigación Biomédica en Red de Fragilidad y Envejecimiento Saludable Instituto de Salud Carlos III, Madrid 28029, Spain; [c]Department of Internal Medicine, Hospital Universitario Royo Villanova, Zaragoza 50015, Spain; [d]Centro Nacional de Investigaciones Cardiovasculares Carlos III, Madrid 28029, Spain; [e]Centro de Neurociencias Cajal, Alcalá de Henares 28805, Spain; [f]Servicio de Cirugía Ortopédica y Traumatología, Hospital Arnau de Vilanova y Hospital de Liria and Health Care Department Arnau-Lliria, Valencia 46015, Spain; [g]Department of Orthopedic Surgery, Clinica Universidad de Navarra, Pamplona 31008, Spain; [h]Centro de Investigación Biomédica en Red de Enfermedades Cardiovasculares Instituto de Salud Carlos III, Madrid 28029, Spain; and [i]Altos Labs, San Diego Institute of Science, San Diego, CA 92121

Author contributions: A.L.S., P.M.-C., J.A.E., and M.C.G.-C. designed research; E.G.-D., C.G.-D., J.L.C.-A., M.d.M.M.-H., P.H.-A., A.C., J.D.-F., E.C., J.V., and M.C.G.-C. performed research; E.G.-D., C.G.-D., J.L.C.-A., M.d.M.M.-H., P.H.-A., J.D.-F., E.C., J.V., A.L.S., P.M.-C., G.O.-G., J.A.E., and M.C.G.-C. analyzed data; and E.G.-D., A.L.S., P.M.-C., G.O.-G., J.A.E., and M.C.G.-C. wrote the paper.

1. L. Rodriguez-Mañas, L. P. Fried, Frailty in the clinical scenario. *Lancet* **385**, e7–e9 (2015).
2. J. Angulo, M. El Assar, L. Rodríguez-Mañas, Frailty and sarcopenia as the basis for the phenotypic manifestation of chronic diseases in older adults. *Mol. Aspects Med.* **50**, 1–32 (2016).
3. A. Álvarez-Bustos *et al.*, Role of sarcopenia in the frailty transitions in older adults: A population-based cohort study. *J. Cachexia Sarcopenia Muscle* **13**, 2352–2360 (2022).
4. C. López-Otín, M. A. Blasco, L. Partridge, M. Serrano, G. Kroemer, Hallmarks of aging: An expanding universe. *Cell* **186**, 243–278 (2022).
5. D. J. Marcinek, L. Ferrucci, Reduced oxidative capacity of skeletal muscle mitochondria is a fundamental consequence of adult ageing. *J. Physiol.* **603**, 17–20 (2024).
6. Y. Lai *et al.*, Multimodal cell atlas of the ageing human skeletal muscle. *Nature* **629**, 154–164 (2024).
7. G. Gouspillou *et al.*, Mitochondrial energetics is impaired *in vivo* in aged skeletal muscle. *Aging Cell* **13**, 39–48 (2014).
8. I. R. Lanza, C. W. Sundberg, J. A. Kent, Reduced oxidative capacity of skeletal muscle is not an inevitable consequence of adult ageing. *J. Physiol.* **603**, 21–24 (2024).
9. D. J. Marcinek *et al.*, Marcinek and Ferrucci response to Lanza et al.. *J. Physiol.* **603**, 25–25 (2024).
10. S. Nóbrega-Pereira *et al.*, G6PD protects from oxidative damage and improves healthspan in mice. *Nat. Commun.* **7**, 10894 (2016).
11. C. Arc-Chagnaud *et al.*, Glucose 6-P dehydrogenase delays the onset of frailty by protecting against muscle damage. *J. Cachexia Sarcopenia Muscle* **12**, 1879–1896 (2021).
12. M. C. Gomez-Cabrera *et al.*, A new frailty score for experimental animals based on the clinical phenotype: Inactivity as a model of frailty. *J. Gerontol. A Biol. Sci. Med. Sci.* **72**, 885–891 (2017).
13. J. Myers *et al.*, Exercise capacity and mortality among men referred for exercise testing. *N. Engl. J. Med.* **346**, 793–801 (2002).
14. M. Bernier *et al.*, Age-dependent impact of two exercise training regimens on genomic and metabolic remodeling in skeletal muscle and liver of male mice. *NPJ Aging* **8**, 8 (2022).

15. P. Srikanthan, A. S. Karlamangla, Relative muscle mass is inversely associated with insulin resistance and prediabetes. Findings from the third National Health and Nutrition Examination Survey. *J. Clin. Endocrinol. Metab.* **96**, 2898–2903 (2011).
16. Z. White *et al.*, Voluntary resistance wheel exercise from mid-life prevents sarcopenia and increases markers of mitochondrial function and autophagy in muscles of old male and female C57BL/6J mice. *Skelet. Muscle* **6**, 45 (2016).
17. S. H. Kim *et al.*, PGC-1α mediates a rapid, exercise-induced downregulation of glycogenolysis in rat skeletal muscle. *J. Physiol.* **593**, 635–643 (2015).
18. L. F. Costa-Machado *et al.*, Peripheral modulation of antidepressant targets MAO-B and GABAAR by harmol induces mitohormesis and delays aging in preclinical models. *Nat. Commun.* **14**, 2779 (2023).
19. MoTrPAC Study Group, Lead Analysts, MoTrPAC Study Group, Temporal dynamics of the multi-omic response to endurance exercise training. *Nature* **629**, 174–183 (2024).
20. P. Venditti, P. Masullo, S. D. Meo, Effect of exercise duration on characteristics of mitochondrial population from rat liver. *Arch. Biochem. Biophys.* **368**, 112–120 (1999).
21. S. Ghosh *et al.*, Reduction in reactive oxygen species production by mitochondria from elderly subjects with normal and impaired glucose tolerance. *Diabetes* **60**, 2051–2060 (2011).
22. J. Viña, G. Olaso-Gonzalez, C. Arc-Chagnaud, A. De Rosa, M. C. Gomez-Cabrera, Modulating oxidant levels to promote healthy aging. *Antioxid. Redox Signal.* **33**, 570–579 (2020).
23. M. C. Gomez-Cabrera, E. Domenech, J. Viña, Moderate exercise is an antioxidant: Upregulation of antioxidant genes by training. *Free Radic. Biol. Med.* **44**, 126–131 (2008).
24. P. J. Fernandez-Marcos, S. Nobrega-Pereira, NADPH: New oxygen for the ROS theory of aging. *Oncotarget* **7**, 50814–50815 (2016).
25. C. Ubaida-Mohien *et al.*, Unbiased proteomics, histochemistry, and mitochondrial DNA copy number reveal better mitochondrial health in muscle of high-functioning octogenarians. *Elife* **11**, e74335 (2022).
26. M. D. Roberts *et al.*, A novel deep proteomic approach in human skeletal muscle unveils distinct molecular signatures affected by aging and resistance training. bioXriv [Preprint] (2023), 10.1101/2023.06.02.543459 (Accessed 14 March 2026).
27. S. Cogliati *et al.*, Mechanism of super-assembly of respiratory complexes III and IV. *Nature* **539**, 579–582 (2016).
28. R. Acín-Pérez, P. Fernández-Silva, M. L. Peleato, A. Pérez-Martos, J. A. Enriquez, Respiratory active mitochondrial supercomplexes. *Mol. Cell* **32**, 529–539 (2008).
29. E. Barca *et al.*, USMG5 Ashkenazi Jewish founder mutation impairs mitochondrial complex V dimerization and ATP synthesis. *Hum. Mol. Genet.* **27**, 3305–3312 (2018).
30. S. P. Stone, B. Ali, I. Auberleek, A. Thompsell, A. Young, The barthel index in clinical practice: Use on a rehabilitation ward for elderly people. *J. R. Coll. Physicians Lond.* **28**, 419–423 (1994).
31. M. E. Charlson *et al.*, The Charlson comorbidity index is adapted to predict costs of chronic disease in primary care patients. *J. Clin. Epidemiol.* **61**, 1234–1240 (2008).
32. S. Subramaniam, J. J. Aalberg, R. P. Soriano, C. M. Divino, New 5-factor modified frailty index using American College of Surgeons NSQIP data. *J. Am. Coll. Surg.* **226**, 173–181.e178 (2018).
33. L. Xing *et al.*, Falls caused by balance disorders in the elderly with multiple systems involved: Pathogenic mechanisms and treatment strategies. *Front. Neurol.* **14**, 1128092 (2023).
34. J. O. Holloszy, Biochemical adaptations in muscle. Effects of exercise on mitochondrial oxygen uptake and respiratory enzyme activity in skeletal muscle. *J. Biol. Chem.* **242**, 2278–2282 (1967).
35. V. R. Kedlian *et al.*, Human skeletal muscle aging atlas. *Nat. Aging* **4**, 727–744 (2024).
36. C. P. Verschoor *et al.*, Alterations to the frequency and function of peripheral blood monocytes and associations with chronic disease in the advanced-age, frail elderly. *PLoS One* **9**, e104522 (2014).
37. L. P. Fried *et al.*, Frailty in older adults: Evidence for a phenotype. *J. Gerontol. A Biol. Sci. Med. Sci.* **56**, M146–M157 (2001).
38. M. C. Gomez-Cabrera *et al.*, Oral administration of vitamin C decreases muscle mitochondrial biogenesis and hampers training-induced adaptations in endurance performance. *Am. J. Clin. Nutr.* **87**, 142–149 (2008).
39. T. A. Hornberger, R. P. Farrar, Physiological hypertrophy of the FHL muscle following 8 weeks of progressive resistance exercise in the rat. *Can. J. Appl. Physiol.* **29**, 16–31 (2004).
40. H. D. Waller, G. W. Lohr, M. Tabatabai, Hemolysis and absence of glucose-6-phosphate dehydrogenase in erythrocytes; An enzyme abnormality of erythrocytes. *Klin. Wochenschr.* **35**, 1022–1027 (1957).
41. E. Fernández-Vizarra *et al.*, Isolation of mitochondria for biogenetical studies: An update. *Mitochondrion* **10**, 253–262 (2010).
42. M. A. Birch-Machin, D. M. Turnbull, Assaying mitochondrial respiratory complex activity in mitochondria isolated from human cells and tissues. *Methods Cell Biol.* **65**, 97–117 (2001).
43. D. M. Kirby, D. R. Thorburn, D. M. Turnbull, R. W. Taylor, Biochemical assays of respiratory chain complex activity. *Methods Cell Biol.* **80**, 93–119 (2007).
44. C. Jung, C. M. Higgins, Z. Xu, Measuring the quantity and activity of mitochondrial electron transport chain complexes in tissues of central nervous system using blue native polyacrylamide gel electrophoresis. *Anal. Biochem.* **286**, 214–223 (2000).
45. J. R. Wiśniewski, A. Zougman, N. Nagaraj, M. Mann, Universal sample preparation method for proteome analysis. *Nat. Methods* **6**, 359–362 (2009).
46. B. C. Orsburn, Proteome Discoverer-a community enhanced data processing suite for protein informatics. *Proteomes* **9**, 15 (2021).
47. U. Consortium, UniProt: The Universal Protein Knowledgebase in 2023. *Nucleic Acids Res.* **51**, D523–D531 (2023).
48. J. C. Wright, J. S. Choudhary, Decoypyrat: Fast non-redundant hybrid decoy sequence generation for large scale proteomics. *J. Proteomics Bioinform.* **9**, 176–180 (2016).
49. A. Keller, A. I. Nesvizhskii, E. Kolker, R. Aebersold, Empirical statistical model to estimate the accuracy of peptide identifications made by MS/MS and database search. *Anal. Chem.* **74**, 5383–5392 (2002).
50. G. Prieto, J. Vázquez, Protein probability model for high-throughput protein identification by mass spectrometry-based proteomics. *J. Proteome Res.* **19**, 1285–1297 (2020).
51. E. Bonzon-Kulichenko, F. Garcia-Marques, M. Trevisan-Herraz, J. Vázquez, Revisiting peptide identification by high-accuracy mass spectrometry: Problems associated with the use of narrow mass precursor windows. *J. Proteome Res.* **14**, 700–710 (2015).
52. P. Navarro *et al.*, General statistical framework for quantitative proteomics by stable isotope labeling. *J. Proteome Res.* **13**, 1234–1247 (2014).
53. F. García-Marqués *et al.*, A novel systems-biology algorithm for the analysis of coordinated protein responses using quantitative proteomics. *Mol. Cell. Proteomics.* **15**, 1740–1760 (2016).
54. J. M. Rodríguez *et al.*, ISanXoT: A standalone application for the integrative analysis of mass spectrometry-based quantitative proteomics data. *Comput. Struct. Biotechnol. J.* **23**, 452–459 (2024).
55. A. Dobin *et al.*, STAR: Ultrafast universal RNA-seq aligner. *Bioinformatics* **29**, 15–21 (2013).
56. B. Li, C. N. Dewey, RSEM: Accurate transcript quantification from RNA-Seq data with or without a reference genome. *BMC Bioinformatics* **12**, 323 (2011).
57. Y. Chen, A. T. Lun, G. K. Smyth, From reads to genes to pathways: Differential expression analysis of RNA-Seq experiments using Rsubread and the edgeR quasi-likelihood pipeline. *F1000Res* **5**, 1438 (2016).
58. M. E. Ritchie *et al.*, Limma powers differential expression analyses for RNA-sequencing and microarray studies. *Nucleic Acids Res.* **43**, e47 (2015).
59. T. Wu *et al.*, ClusterProfiler 4.0: A universal enrichment tool for interpreting omics data. *Innovation* **2**, 100141 (2021).
60. S. Rath *et al.*, MitoCarta3.0: An updated mitochondrial proteome now with sub-organelle localization and pathway annotations. *Nucleic Acids Res.* **49**, D1541–D1547 (2021).
61. E. García-Domínguez *et al.,* Mitochondrial remodeling in skeletal muscle underlies exercise-induced reversal of age-associated functional decline in mice and humans. NCBI Gene Expression Omnibus. https://www.ncbi.nlm.nih.gov/geo/query/acc.cgi?acc=GSE325919. Deposited 26 March 2026.
62. E. García-Domínguez *et al.,* Mitochondrial remodeling in skeletal muscle underlies exercise-induced reversal of age-associated functional decline in mice and humans. PRoteomics IDEntifications Database. https://www.ebi.ac.uk/pride/archive/projects/PXD076192. Deposited 26 March 2026.